CAMBRIDGE
UNIVERSITY PRESS

Mineralogical Society

Article

Density functional theory study of the atomic and electronic structures of *trans*-vacant 1*M* Al-rich illite

Wei Gao[1,2], Jian Zhao[1,2] (iD) and Man-Chao He[1,2]

[1]State Key Laboratory of Geomechanics and Deep Underground Engineering, China University of Mining and Technology, Beijing, China and [2]School of Mechanics and Civil Engineering, China University of Mining and Technology-Beijing, Beijing, China

Abstract

Illite is a common clay mineral that is found in a wide range of geological settings. The good thermal stability and non-swelling properties of illite make it valuable in ceramic materials, paints and coatings, drilling fluids, agriculture and geological studies. To gain a deeper understanding of the physical and chemical properties of illite, in the present paper the atomic and electronic structures of a typical *trans*-vacant 1*M* Al-rich illite were constructed and calculated using density functional theory. The calculated indirect band gap of Al-rich illite was 4.99 eV. The electronic analysis revealed that the interactions in the tetrahedral sheet were more stable than those in the octahedral sheet. The substitution of Al atoms noticeably reduced the stability of the tetrahedral sheet in Al-rich illite. Other properties of Al-rich illite, including the density of states, electron population/charge, electronic charge density and bonding interaction, are also discussed and analysed in detail.

Illite is a type of mica-like phyllosilicate clay mineral. Its name was introduced by Grim *et al.* (1937) and derived from the name of the state of Illinois, USA. Illite is a widespread mineral found in diverse geological environments, primarily originating from the weathering and alteration of other minerals such as micas and feldspars (Righi & Meunier, 1995; Shoval, 2023). The good thermal stability (He *et al.*, 1995) and non-swelling properties (Ruiz Pestana *et al.*, 2017) of illite make it valuable in a wide range of industrial and geological applications, including ceramic materials, paints and coatings, drilling fluids, agriculture and geological studies (Steiger, 1982; Feng *et al.*, 1999; Sedmale *et al.*, 2017; Li *et al.*, 2018; Zhang *et al.*, 2020; El Halim *et al.*, 2022).

Existing experimental and theoretical data have confirmed the 2:1-type dioctahedral layered structure of illite, which consists of stacked layers primarily bound by van der Waals forces (Brigatti & Guggenheim, 2002). An individual 2:1 basic layer comprises two tetrahedral sheets sandwiching one octahedral sheet to form a T–O–T structure (Bergaya & Lagaly, 2013). The tetrahedral sheets are composed of Si–O tetrahedrons with some of the Si atoms substituted by Al atoms, whereas the octahedral sheet consists of Al, Mg or Fe cations coordinated with OH groups (Meunier & Velde, 2004). The interlayer space of illite primarily accommodates K ions, and the interlayer charge generally ranges between 0.60 and 0.85 per $O_{10}(OH)_2$ (Rieder *et al.*, 1998). The octahedral sheet of illite exhibits two types of structure – *cis*-vacant and *trans*-vacant – determined by the configuration of the

coordinating OH groups (Drits *et al.*, 2006; Drits *et al.*, 2012). In terms of polytypes, it has been observed that the 1*M* and 2*M*₁ polytypes are most frequently encountered in illite species (Zoeller & Brockamp, 1997; Zviagina & Drits, 2019).

Due to the complexity of the chemical components, disordered stacking, cation substitutions, cation configurations and the small crystalline domain size of illite, measuring its atomic structure and crystal properties accurately through experiments remains challenging. With advancements in theoretical research, computational chemistry calculations based on density functional theory (DFT) have been proven to be effective and reliable for investigating clay minerals at the molecular level (Bridgeman, 1996; Beermann & Brockamp, 2005; Mercier *et al.*, 2010; He *et al.*, 2012; Teich-McGoldrick *et al.*, 2012; Scholtzová & Tunega, 2019; Yuan *et al.*, 2022; Zhao *et al.*, 2023). A series of studies has investigated the structure of illite using DFT. Stixrude & Peacor (2002) discussed two avaliable competing models of illite smectite systems based on a first-principles study. The results revealed that differences in energy and structure between the two models can be understood in terms of local charge balance. Militzer *et al.* (2011) calculated the elastic constants of muscovite illite–smectite using DFT theory, and the differences indicated that there were variations in their crystal sturctures. Geatches & Wilcox (2014) modelled a variety of interlayer-deficient dioctahedral mica models of the 1*M* illite series based on crystallographic data and average formulae with DFT, and they analyzed the differences between *cis*-vacant and *trans*-vacant models. Escamilla-Roa *et al.* (2016) investigated the stability of the hydronium cation in the structure of illite. The results revealed that the hydronium cation remains in the interlayer of illite at high temperatures. Sánchez-Coronilla *et al.* (2019) investigated the inclusion of Fe, Cu and Zn in Illite. After analysing the

stability and electronic effect of the inclusion system, illite presented good adsorption characteristics for Fe, Cu and Zn in the (1,0,0) site.

In the present paper, a DFT study of a typical *trans*-vacant 1*M* Al-rich illite without octahedral substitution is reported by calculating its atomic and electronic structure, density of states (DOS), electron population/charge, electronic charge density and bonding interaction analysis. The current DFT results will contribute to a better understanding of the chemical, physical and mechanical properties of illite from a microscopic perspective.

Method of calculation

The periodic DFT calculations were conducted with the Vienna *ab initio* simulation package (*VASP*; Monkhorst & Pack, 1976; Kresse & Furthmüller, 1996). The interaction between the ions and valence electrons is described by the full-potential frozen-core all-electron projector augmented wave (PAW) method proposed by Blöchl (1994) and by Kresse & Joubert (1999). Plane-wave pseudopotentials and periodic boundary conditions were applied when solving the Kohn–Sham DFT equations. The electron exchange potential and correlation energy were calculated using the Perdew–Burke–Ernzerhof (PBE) form of the generalized gradient approximation (GGA; Perdew *et al.*, 1996). In the present paper, a ($3 \times 4 \times 3$) Monkhorst–Pack k-point was utilized for Brillouin-zone integrations. The corresponding plane-wave basis cutoff energy was set at 450 eV. Geometry optimization was terminated when the Hellman–Feynman forces acting on each atom fell below 0.01 eV Å^{-1}, and the self-consistency iterations concluded once the total energies converged to within 10^{-4} eV. The valence electron configurations of the elements in Al-rich illite were determined to be H $1s^1$, O $2s^2 2p^4$, Al $3s^2 3p^1$, Si $3s^2 3p^2$ and K $3s^2 3p^6 4s^1$. The accuracy of the calculations for weak interactions was ensured by employing the DFT-D3 dispersion correction method (Moellmann & Grimme, 2014).

The Mulliken population/charge calculations and crystal orbital Hamilton population (COHP) bonding analyses were conducted using the *LOBSTER* package (Hughbanks & Hoffmann, 1983; Dronskowski & Bloechl, 1993; Maintz *et al.*, 2016; Ertural *et al.*, 2019). Basis sets given by Koga and Maintz that fitted to the atomic *VASP* GGA-PBE wavefunctions were employed during the projection (Koga *et al.*, 2000).

Results and discussion

The system of $K_xAl_2(Si_{4-x}Al_x)O_{10}(OH)_2$ was used to determine the chemical formula of Al-rich illite. The values of x ranged from 0.60 to 0.85, which conformed to the required layer charge and lattice substitution ratio. Based on the chemical composition analysis of Al-rich illite samples (Drits *et al.*, 2010), in the present paper $x = 0.75$, for the ideal chemical formula of $K_{0.75}Al_2(Si_{3.25}Al_{0.75})O_{10}(OH)_2$, was selected to represent a type of Al-rich illite. The initial cell configuration of the Al-rich illite was derived from the illite cells constructed by Drits *et al.* (2010) and consisted of a *trans*-vacant dioctahedral 1*M* polytype structure. K ions were introduced in the interlayer to balance the cell charge. Subsequently, Si atoms in the Si–O tetrahedrons were substituted with Al atoms to afford the $K_3Al_8(Si_{13}Al_3)O_{40}(OH)_8$ chemical formula. The configurations of the three substituted tetrahedral Al atoms were analysed comprehensively through calculations as presented in Table 1. To provide a clearer and more intuitive demonstration of the configurations of the three substituted Al atoms, a selection of representative configurations was

Table 1. The calculated total energy of the Al-rich illite with different configurations of the three substituted tetrahedral Al atoms.

Configuration	Energy (eV)	Configuration	Energy (eV)
a	−596.33	m	−596.21
b	−596.22	n	−596.20
c	−596.21	o	−596.16
d	−596.20	p	−596.16
e	−596.19	q	−596.02
f	−596.05	r	−596.01
g	−595.93	s	−595.98
h	−595.84	t	−595.88
i	−595.78	u	−595.83
j	−595.32	v	−595.80
k	−595.12	w	−595.72
l	−595.05	x	−595.60

chosen, and these are presented (arranged in order of energy) in Fig. 1. Lower energy corresponds to a more stable structure. The results revealed that the local aggregation of Al–O tetrahedrons result in reduced stability of the Al-rich illite cell, which was related to the partial local balance between the interlayer charge and the charge-deficient tetrahedral sheets (Stixrude & Peacor, 2002).

The final optimized crystal structure model of Al-rich illite (with the most stable configuration of substituted tetrahedral Al atoms) is presented in Fig. 2a. The calculated structural parameters were: $2a = 10.454$ Å, $b = 9.021$ Å, $c = 10.316$ Å, $\alpha = 89.93°$, $\beta = 101.99°$ and $\gamma = 89.92°$, which were in good agreement with the existing experimental data (Eberl *et al.*, 1987; Drits & McCarty, 2007), as shown in Table 2. The major bond lengths of Al-rich illite are presented in Table 3. Considering the difference in symmetries and positions, as indicated in Fig. 2b, the Al atoms were divided into two kinds: Al_a was an Al atom in an octahedral sheet; and Al_b was a substituted Al atom in a tetrahedral sheet. The O atoms were divided into five kinds: O_a was an O atom of the hydroxyl in an octahedral sheet; O_b was an inner O atom shared by a Si–O tetrahedron and an Al–O octahedron; O_c was an inner O atom shared by an Al–O tetrahedron and an Al–O octahedron; O_d was an O atom in a tetrahedral sheet connected between Si and Al_b; and O_e was an O atom in a tetrahedral sheet connected between Si atoms. The results revealed that the length of the bonds in a octahedral sheet (Al_a–O_a, Al_a–O_b and Al_a–O_c) were all longer than those of the bonds in a tetrahedral sheet (Si–O_b, Al_b–O_c, Si–O_e, Al_b–O_d and Si–O_d), which implied that the bonding interactions in an octahedral sheet were weaker than those in a tetrahedral sheet. The lengths of the bonds in a Si–O tetrahedron (Si–O_e, Si–O_b and Si–O_d) were all shorter than those of the bonds in an Al–O tetrahedron (Al_b–O_c and Al_b–O_d), which indicated that the substitution of Al atoms reduced the connection strength of a tetrahedral sheet.

Figure 3 displays the band structure of Al-rich illite near the Fermi level. The high-symmetry Brillouin-zone points were G (0,0,0), F(0,0.5,0), Q(0,0.5,0.5) and Z(0,0,0.5). The conduction-band minimum of Al-rich illite is at the G point and the valence-band maximum is at the F point. Thus, Al-rich illite was calculated to have an indirect band gap with a gap width of 4.99 eV. This characteristic illustrated that Al-rich illite can be treated as an insulator.

To further investigate the electronic properties of Al-rich illite, the electronic total DOS (TDOS) and electronic partial DOS (PDOS) for H, O, Al, Si and K atoms were calculated, and these are presented in Fig. 4. Five types of O atom and two
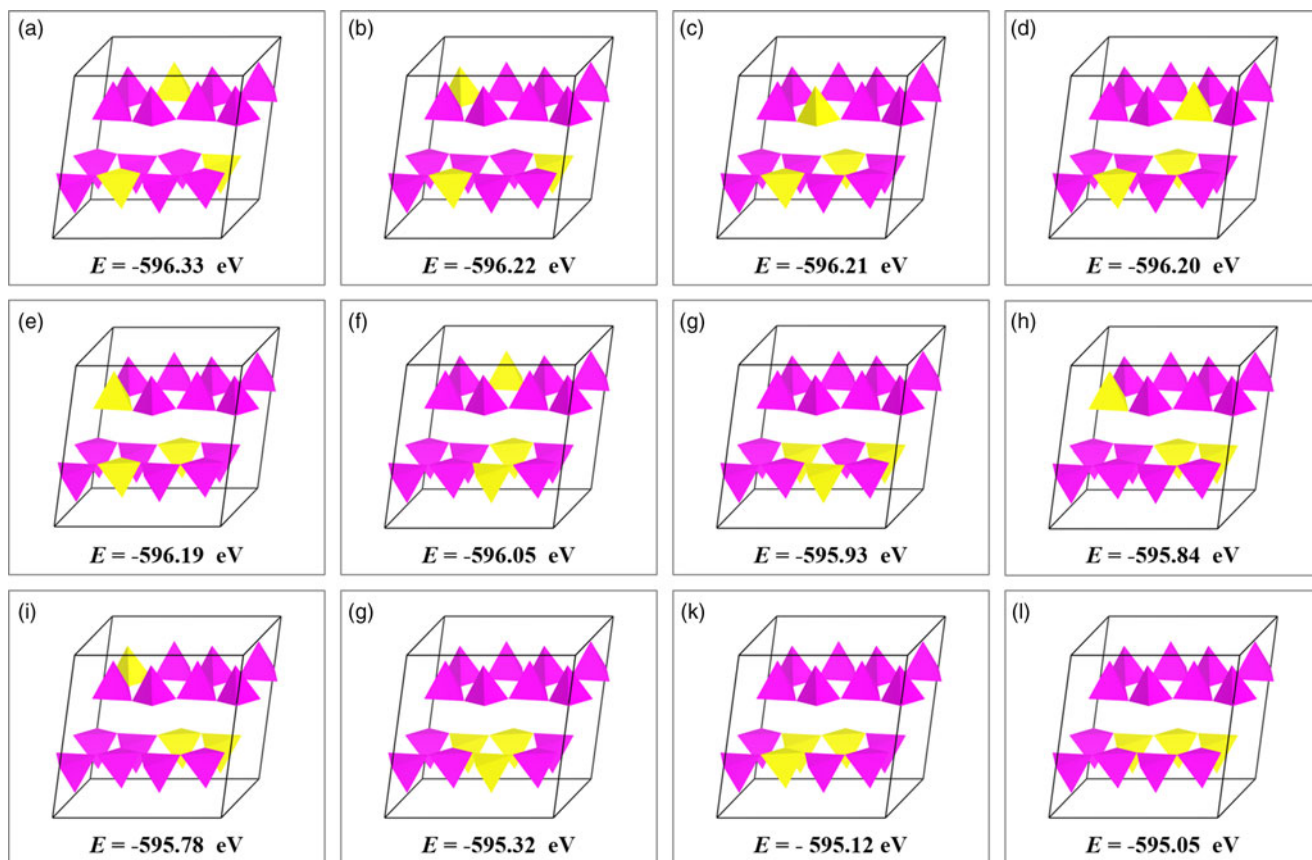
Figure 1. A selection of representative configurations of 13 Si atoms and three substituted Al atoms (shown as tetrahedra) in the Al-rich illite unit cell. (a–l) Representative configurations of Al–O tetrahedra and Si–O tetrahedra arranged in order of energy. Yellow tetrahedra = Al–O tetrahedra; pink tetrahedra = Si–O tetrahedra.
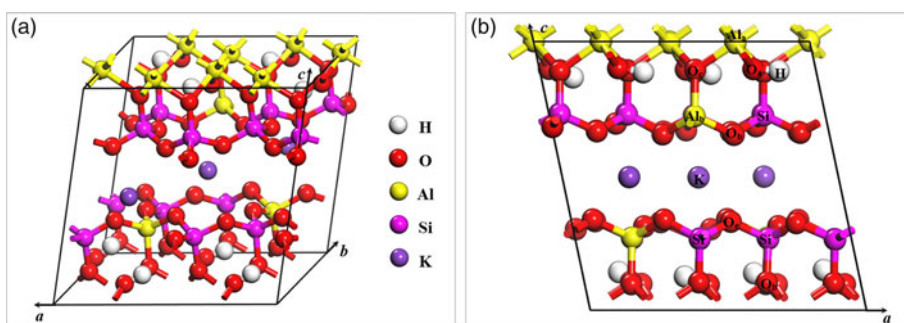

Figure 2. Crystal structures of the Al-rich illite $K_3Al_8(Si_{13}Al_3)O_{40}(OH)_8$. (a) Unit cell of Al-rich illite. (b) Characteristic atoms and bonds in Al-rich illite (back view). White spheres = hydrogen; red spheres = oxygen; yellow spheres = aluminium; pink spheres = silicon; purple spheres = potassium.

Table 2. Calculated and experimental lattice parameters of the Al-rich illite.

Phase	$2a$ (Å)	b (Å)	c (Å)	α (°)	β (°)	γ (°)
Present study	10.455	9.022	10.316	89.94	101.99	89.92
Experimental[a]	10.399	8.982	10.233	90.00	101.60	90.00
Experimental[b]	10.404	8.980	10.227	90.00	101.57	90.00

[a]Eberl *et al.* (1987).
[b]Drits & McCarty (2007).

Table 3. Calculated bond lengths in the optimized structure of the Al-rich illite.

Bond	$H–O_a$	$Al_a–O_a$	$Al_a–O_b$	$Al_a–O_c$	$Al_b–O_c$	$Al_b–O_d$	$Si–O_b$	$Si–O_d$	$Si–O_e$
Length (Å)	0.973	1.928	1.951	1.889	1.752	1.759	1.643	1.607	1.647

types of Al atom were individually plotted, taking into account their symmetries and positions. The Fermi energy was set at 0. The TDOS within the energy range of –35 to 0 eV exhibited four prominent peaks, labelled as 1–4 in Fig. 4a,a′. It is clear that peaks 1 and 3 were solely contributed by the K *s* and *p* states. Peak 2 was mainly from the O 2*s* state, with a partial contribution of Si and Al 3*s*/3*p* and H 1*s* states. By contrast, peak 4 was almost entirely contributed by the 2*p* state of O atoms. After integrating the band structures in Fig. 3, it became evident that the top of the valence band is primarily composed of the 2*p* state of O atoms, whereas the bottom of the conduction band includes the 3*s*/3*p*
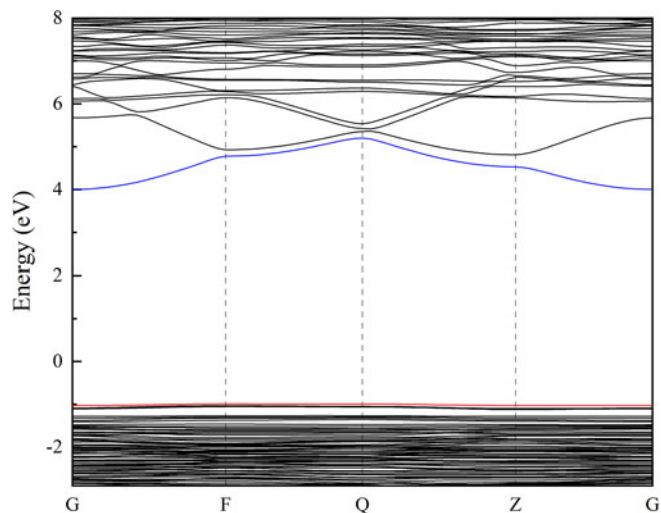
Figure 3. Calculated band structure for the Al-rich illite. The red and blue lines represent the bottom of the conduction band and the top of the valence band, respectively.

Table 4. Atomic Mulliken population/charge analysis and COHP bonding analysis for characteristic atoms and bonds in the Al-rich illite.

Atom	s	p	Total	Charge (e)	Bond	ICOHP (eV)	Length (Å)
K	1.99	6.00	7.99	1.01	K–O_d	−0.21	2.80
Al_a	0.49	0.88	1.38	1.62	H–O_b	−8.37	0.97
Al_b	0.44	0.83	1.27	1.73	Al_a–O_a	−4.17	1.93
Si	0.58	1.24	1.82	2.18	Al_a–O_b	−3.96	1.95
H	0.58	0	0.58	0.42	Al_b–O_c	−5.47	1.75
O_a	1.80	5.17	6.96	−0.96	Al_b–O_d	−5.83	1.76
O_b	1.81	5.28	7.09	−1.09	Si–O_b	−7.63	1.64
O_c	1.81	5.32	7.13	−1.13	Si–O_d	−8.36	1.61
O_d	1.82	5.34	7.16	−1.16	Si–O_e	−7.63	1.65
O_e	1.81	5.34	7.15	−1.15			

states of Si and Al atoms. Five different types of O atom exhibited similar PDOS curves, which are attributed to the high ionicity of the oxygen, resulting in charge transfer from adjacent H, Al and Si atoms. As shown in Fig. 4b,c,g, the overlap between the O_b 2s state and H 1s state split into two peaks due to the hybridization with Al_a 3s/3p states in the octahedral sheet. Similarly, a particularly narrow peak of the O 1s state arose in the PDOS plot of O_c (Fig. 4c), which contributed peak 2′ of the TDOS plot. In the tetrahedral sheet, as shown in Fig. 4d,e,h–k, the substituted Al_b atom presented a different hybrid mode with adjacent O atoms compared to the Si atom. It is clear that the degree of hybridization between the Si 3p state and the adjacent O 2p state was stronger than that between the Al_b 3p state and adjacent the O 2p state.

The atomic Mulliken population/charge analysis and the COHP bonding analysis for characteristic atoms and bonds in Al-rich illite were implemented using the *LOBSTER* package, and these are summarized in Tables 4 & 5. The Mulliken charge populations provide a comprehensive quantification of the charge transfers occurring within the crystals. The results revealed that five types of O atom gained 0.96–1.16 e, while the adjacent K lost 1.01 e, H lost 0.42 e, Si lost 2.18 e, Al_b lost 1.73 e and Al_a lost 1.62 e. In the tetrahedral sheet, the Si atom lost more electrons than the substituted Al_b atom, which indicated a stronger charge transfer between the Si atom and adjacent O atoms. Moreover, the residual electrons in the Al 3s/3p and Si 3s/3p states revealed the covalent character of the Si–O and Al–O bonds in the tetrahedrons and octahedrons. COHP can reveal the nature of covalent interactions between bonding atoms, whereas the integrated COHP (ICOHP) values up to the Fermi-level yields are the bond contributions to the band-structure energy, which provides clues as to the bond strength. The calculated ICOHP values of the bonds Al_a–O_a, Al_a–O_b, Si–O_b, Al_b–O_c, Si–O_e, Al_b–O_d and Si–O_d were −4.17, −3.96, −7.63, −5.47, −7.63, −5.83 and −8.36 eV, respectively, indicating that the bonding interaction strength of these bonds followed the order Si–O_d > Si–O_b > Si–O_e > Al_b–
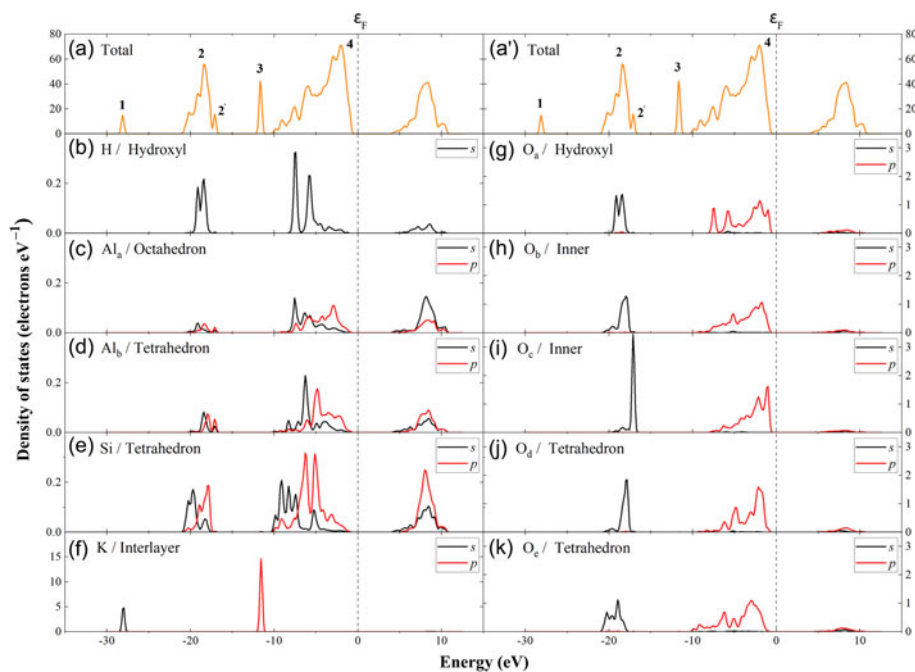

Figure 4. The calculated electronic TDOS and electronic PDOS for the H, O, Al, Si and K atoms of the Al-rich illite. (a & a′) TDOS of the Al-rich illite. (b) PDOS of the H atom in the hydroxyl. (c) PDOS of the Al_a atom in the octahedron. (d) PDOS of the substituted Al_b atom in the tetrahedron. (e) PDOS of the Si atom in the tetrahedron. (f) PDOS of the interlayer K atom. (g) PDOS of the O_a atom in the hydroxyl. (h) PDOS of the inner O_b atom. (i) PDOS of the inner O_c atom. (j) PDOS of the O_d atom connected between the Si and Al_b atoms. (k) PDOS of the O_e atom connected between Si atoms.

Table 5. Atomic Mulliken population analysis with specific orbitals for characteristic atoms of the Al-rich illite.

Atom	O_a		O_b		O_c		O_d	
Mulliken populations	$2s$	1.80	$2s$	1.81	$2s$	1.81	$2s$	1.82
	$2p\_y$	1.76	$2p\_y$	1.82	$2p\_y$	1.81	$2p\_y$	1.79
	$2p\_z$	1.82	$2p\_z$	1.71	$2p\_z$	1.77	$2p\_z$	1.80
	$2p\_x$	1.59	$2p\_x$	1.75	$2p\_x$	1.74	$2p\_x$	1.75
	Total	6.96	Total	7.09	Total	7.13	Total	7.16

Atom	O_e		Al_a		Al_b		Si	
Mulliken populations	$2s$	1.81	$3s$	0.49	$3s$	0.44	$3s$	0.58
	$2p\_y$	1.79	$3p\_y$	0.30	$3p\_y$	0.28	$3p\_y$	0.43
	$2p\_z$	1.82	$3p\_z$	0.31	$3p\_z$	0.28	$3p\_z$	0.41
	$2p\_x$	1.73	$3p\_x$	0.27	$3p\_x$	0.27	$3p\_x$	0.40
	Total	7.15	Total	1.38	Total	1.27	Total	1.82

$O_d > Al_b–O_c > Al_a–O_a > Al_a–O_b$. The results revealed that, in the tetrahedral sheet, the Si–O bonds were significantly stronger than the Al–O bonds, suggesting that the substitution of Al_b weakened the stability of the silica tetrahedra. However, the Si–O and Al–O bonds in the tetrahedral sheet were all stronger than the Al–O bond in the octahedral sheet, indicating that the tetrahedral sheet was more stable than the octahedral sheet, even in the presence of substitution.

To gain a greater understanding of the bonding properties and charge distributions of the atoms in the tetrahedral sheet of Al-rich illite, the 3D and 2D electronic charge density contour plots (Fig. 5) were sampled within the plane containing the Si, Al_b and O_d atoms, which were positioned at the centre of the diagram. To better observe the charge density variation between atoms, regions with an electronic charge density exceeding $1\ e\ Å^{-3}$ were coloured white. The results revealed that the charge density around the O_d atom was substantial, indicating the high electronegativity of the O atom. The overlap of charge density within the Si–O_d and Al_b–O_d bond regions indicated covalent bonding properties. The dense contour lines within the Si–O_d bond region implied a stronger covalent bonding interaction compared to the Al_b–O_d bond, which is consistent with the conclusions presented above. Furthermore, the sparse contour lines around the Al_b atom revealed an ionic bonding characteristic of
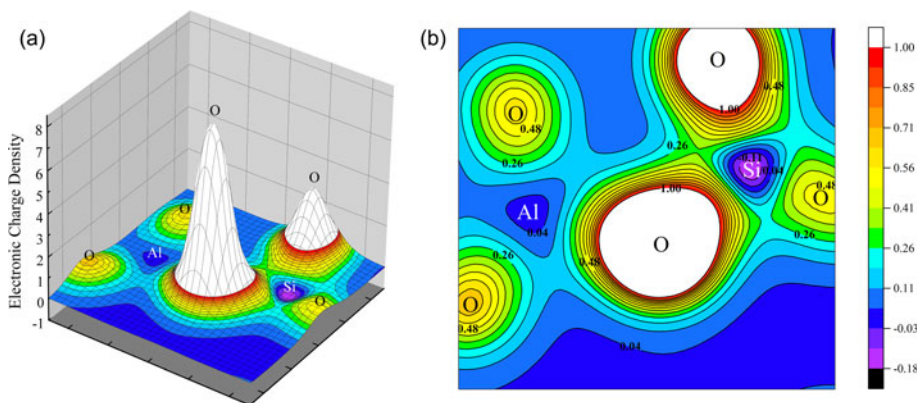
Figure 5. The sampled (a) 3D and (b) 2D electronic charge density contour plots of the Al-rich illite.
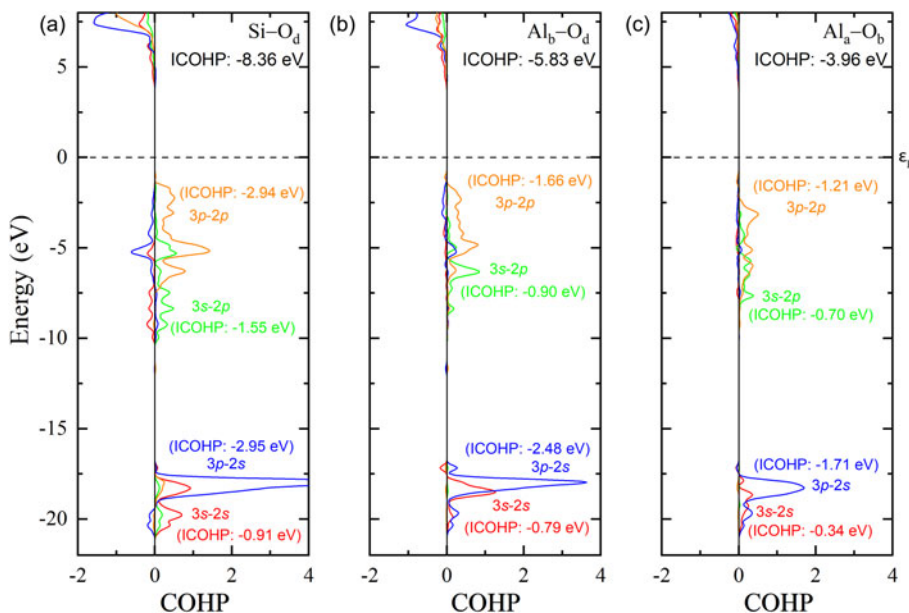
Figure 6. The COHP analyses including the main orbital-pair contributions for three types of bonds of the Al-rich illite: (a) the Si–O_d bond in the tetrahedral sheet; (b) the Al_b–O_d bond in the tetrahedral sheet; and (c) the Al_a–O_b bond in the octahedral sheet.

the Al$_b$–O$_d$ bond. This mixed ionic/covalent bonding property has also been discovered in other clay minerals such as kaolinite and montmorillonite.

Further COHP analyses including main orbital-pair contributions were performed to investigate the bonding interactions of Si–O$_d$, Al$_b$–O$_d$ and Al$_a$–O$_b$, as shown in Fig. 6. A comparison of the Si–O$_d$ bond (ICOHP = –8.36 eV) and Al$_b$–O$_d$ bond (ICOHP = –5.83 eV) in the tetrahedral sheet (Fig. 6a,b) revealed that all of the interactions (3s–2s, 3s–2p, 3p–2s and 3p–2p) of the Si–O$_d$ bond were enhanced compared to the Al$_b$–O$_d$ bond. Particularly noteworthy was the 3p–2p orbital pair (ICOHP = –2.94 eV), which reached a similar characteristic strength level as the 3p–2s orbital pair (ICOHP = –2.95 eV). The results revealed a high degree of hybridization between the orbitals of the Si and O$_d$ atoms, especially the Si 3p and O$_d$ 2s/2p states. Some 3p/3s–2s antibonding states were found in the energy range from –10 to –3 eV for the Si–O$_d$ bond, which somewhat attenuated the interactions of the 3p–2s and 3s–2p bonding characteristics. Furthermore, a comparison of Al$_a$–O$_b$ bond (ICOHP = –3.96 eV) interaction strengths and the main orbital-pair contribution is also presented in Fig. 6c. It was observed that the Al$_a$–O$_b$ bond in octahedra presented weaker bonding interactions in all orbital pairs compared to the Al$_b$–O$_d$ and Si–O$_d$ bonds in tetrahedra, which resulted in lower structural stability of the octahedral sheet compared to the tetrahedral sheet.

Conclusion

In the present study, the atomic structure of a typical *trans*-vacant 1*M* Al-rich illite was constructed and systematically investigated using the DFT method. The calculated structural parameters were in good agreement with the available experimental values. The calculated indirect band gap of Al-rich illite was 4.99 eV, and as a result it can be treated as an insulator. The bond-length analyses indicated that the interactions in the tetrahedral sheet were more stable than those in the octahedral sheet. The ICOHP values of the Si–O and Al–O bonds in the tetrahedral sheet were –8.36 and –5.83 eV, respectively, which indicated that the substitutions of Al atoms reduced the stability of the tetrahedral sheet. The electronic charge density implied a mixed ionic/covalent bonding property in Al-rich illite. The present findings serve as a valuable reference for use in experimental and theoretical mineralogical investigations into illite.

Conflicts of interest. The authors declare none.

References

Beermann T. & Brockamp O. (2005) Structure analysis of montmorillonite crystallites by convergent-beam electron diffraction. *Clay Minerals*, **40**, 1–13.

Bergaya F. & Lagaly G. (2013) *Handbook of Clay Science*, 2nd edition. Elsevier, Amsterdam, The Netherlands, 1752 pp.

Blöchl P.E. (1994) Projector augmented-wave method. *Physical Review B*, **50**, 17953–17979.

Bridgeman C.H. (1996) *Ab-initio* total energy study of uncharged 2:1 clays and their interaction with water. *Molecular Physics*, **89**, 879–888.

Brigatti M.F. & Guggenheim S. (2002) Mica crystal chemistry and the influence of pressure, temperature, and solid solution on atomistic models. *Reviews in Mineralogy and Geochemistry*, **46**, 1–97.

Drits V.A. & McCarty D.K. (2007) The nature of structure-bonded H$_2$O in illite and leucophyllite from dehydration and dehydroxylation experiments. *Clays and Clay Minerals*, **55**, 45–58.

Drits V.A., McCarty D.K. & Zviagina B.B. (2006) Crystal-chemical factors responsible for the distribution of octahedral cations over *trans*- and *cis*-sites in dioctahedral 2:1 layer silicates. *Clays and Clay Minerals*, **54**, 131–152.

Drits V.A., Zviagina B.B., McCarty D.K. & Salyn A.L. (2010) Factors responsible for crystal-chemical variations in the solid solutions from illite to aluminoceladonite and from glauconite to celadonite. *American Mineralogist*, **95**, 348–361.

Drits V.A., McCarty D.K. & Derkowski A. (2012) Mixed-layered structure formation during *trans*-vacant Al-rich illite partial dehydroxylation. *American Mineralogist*, **97**, 1922–1938.

Dronskowski R. & Bloechl P.E. (1993) Crystal orbital hamilton populations (COHP): energy-resolved visualization of chemical bonding in solids based on density-functional calculations. *Journal of Physical Chemistry*, **97**, 8617–8624.

Erertal C., Steinberg S. & Dronskowski R. (2019) Development of a robust tool to extract Mulliken and Löwdin charges from plane waves and its application to solid-state materials. *RSC Advances*, **9**, 29821–29830.

Escamilla-Roa E., Nieto F. & Sainz-Díaz C.I. (2016) Stability of the hydronium cation in the structure of illite. *Clays and Clay Minerals*, **64**, 413–424.

Feng X., Faiia A.M., WoldeGabriel G., Aronson J.L., Poage M.A. & Chamberlain C.P. (1999) Oxygen isotope studies of illite/smectite and clinoptilolite from Yucca Mountain: implications for paleohydrologic conditions. *Earth and Planetary Science Letters*, **171**, 95–106.

Geatches D.L. & Wilcox J. (2014) *Ab initio* investigations of dioctahedral interlayer-deficient mica: modelling 1*M* polymorphs of illite found within gas shale. *European Journal of Mineralogy*, **26**, 127–144.

Grim R.E., Bray R.H. & Bradley W.F. (1937) The mica in argillaceous sediments. *American Mineralogist*, **22**, 813–829.

He C., Makovicky E. & Øsbæck B. (1995) Thermal stability and pozzolanic activity of calcined illite. *Applied Clay Science*, **9**, 337–354.

He M.-C., Zhao J. & Fang Z.-J. (2012) First-principles study of atomic and electronic structures of kaolinite in soft rock. *Chinese Physics B*, **21**, 039101.

Hughbanks T. & Hoffmann R. (1983) Chains of *trans*-edge-sharing molybdenum octahedra: metal–metal bonding in extended systems. *Journal of the American Chemical Society*, **105**, 3528–3537.

Koga T., Kanayama K., Watanabe T., Imai T. & Thakkar A.J. (2000) Analytical Hartree–Fock wave functions for the atoms Cs to Lr. *Theoretical Chemistry Accounts*, **104**, 411–413.

Kresse G. & Furthmüller J. (1996) Efficient iterative schemes for *ab initio* total-energy calculations using a plane-wave basis set. *Physical Review B*, **54**, 11169.

Kresse G. & Joubert D. (1999) From ultrasoft pseudopotentials to the projector augmented-wave method. *Physical Review B*, **59**, 1758.

Li H., Ou J., Wang X., Yan Z. & Zhou Y. (2018) Immobilization of soil cadmium using combined amendments of illite/smectite clay with bone chars. *Environmental Science and Pollution Research*, **25**, 20723–20731.

Maintz S., Deringer V.L., Tchougréeff A.L. & Dronskowski R. (2016) LOBSTER: a tool to extract chemical bonding from plane-wave based DFT. *Journal of Computational Chemistry*, **37**, 1030–1035.

Mercier P.H.J., Le Page Y. & Desgreniers S. (2010) Kaolin polytypes revisited *ab initio* at 10 GPa. *American Mineralogist*, **95**, 1117–1120.

Meunier A. & Velde B. (2004) The mineralogy of illite – what is illite? Pp. 3–62 in: *Illite: Origins, Evolution and Metamorphism* (A. Meunier & B. Velde, editors). Springer, Berlin, Germany.

Militzer B., Wenk H.-R., Stackhouse S. & Stixrude L. (2011) First-principles calculation of the elastic moduli of sheet silicates and their application to shale anisotropy. *American Mineralogist*, **96**, 125–137.

Moellmann J. & Grimme S. (2014) DFT-D3 study of some molecular crystals. *Journal of Physical Chemistry C*, **118**, 7615–7621.

Monkhorst H.J. & Pack J.D. (1976) Special points for Brillouin-zone integrations. *Physical Review B*, **13**, 5188–5192.

Perdew J.P., Burke K. & Ernzerhof M. (1996) Generalized gradient approximation made simple. *Physical Review Letters*, **77**, 3865–3868.

Rieder M., Cavazzini G., D'Yakonov Y.S., Frank-Kamenetskii V.A., Gottardi G., Guggenheim S. *et al.* (1998) Nomenclature of the micas. *Clays and Clay Minerals*, **46**, 586–595.

Righi D. & Meunier A. (1995) Origin of clays by rock weathering and soil formation. Pp. 43–161 in: *Origin and Mineralogy of Clays: Clays and the Environment* (B. Velde, editor). Springer, Berlin, Germany.

Ruiz Pestana L., Kolluri K., Head-Gordon T. & Lammers L.N. (2017) Direct exchange mechanism for interlayer ions in non-swelling clays. *Environmental Science & Technology*, **51**, 393–400.

Sánchez-Coronilla A., Martín E.I., Fernández-de-Cordova F.J., Santos F.J. & Toledo J.H. (2019) A theoretical study on the inclusion of Fe, Cu, and Zn in illite clays. *Journal of Nanomaterials*, **2019**, 4546350.

Scholtzová E. & Tunega D. (2019) Density functional theory study of the stability of the tetrabutylphosphonium and tetrabutylammonium montmorillonites. *Clay Minerals*, **54**, 41–48.

Sedmale G., Randers M., Rundans M. & Seglins V. (2017) Application of differently treated illite and illite clay samples for the development of ceramics. *Applied Clay Science*, **146**, 397–403.

Shoval S. (2023) Characterization of the clayey sediments in the environment of exposed mudflats on the western dead sea shore. *Clay Minerals*. https://doi.org/10.1180/clm.2023.33.

Steiger R.P. (1982) Fundamentals and use of potassium/polymer drilling fluids to minimize drilling and completion problems associated with hydratable clays. *Journal of Petroleum Technology*, **34**, 1661–1670.

Stixrude L. & Peacor D.R. (2002) First-principles study of illite–smectite and implications for clay mineral systems. *Nature*, **420**, 165–168.

Teich-McGoldrick S.L., Greathouse J.A. & Cygan R.T. (2012) Molecular dynamics simulations of structural and mechanical properties of muscovite: pressure and temperature effects. *Journal of Physical Chemistry C*, **116**, 15099–15107.

Yuan R., Wang W.-M., He Y., Fang Y. & Huang X.-L. (2022) Molecular dynamics modelling of Na-montmorillonite subjected to uniaxial compression and unidirectional shearing. *Clay Minerals*, **57**, 241–252.

Zhang J.R., Xu M.D., Christidis G.E. & Zhou C.H. (2020) Clay minerals in drilling fluids: functions and challenges. *Clay Minerals*, **55**, 1–11.

Zhao J., Wang Y.-F., Luan Z.-L., Cao Y. & He M.-C. (2023) Theoretical analysis of the effect of doping with Na(I), K(I), Mg(II), Ca(II) and Fe(II) on the electronic and mechanical properties of pyrophyllite. *Clay Minerals*, **58**, 113–120.

Zoeller M. & Brockamp O. (1997) $1M$- and $2M_1$-illites: different minerals and not poly types. *European Journal of Mineralogy*, **9**, 821–828.

Zviagina B.B. & Drits V.A. (2019) Structural factors affecting the crystal-chemical variability in Al-rich K-dioctahedral $2M_1$ micas. *Clay Minerals*, **54**, 169–179.